Thresholds of absolute instabilities driven by a broadband laser

R. K. Follett,[1] J. G. Shaw,[1] J. F. Myatt,[2] C. Dorrer,[1] D. H. Froula,[1] and J. P. Palastro[1]
[1)]*Laboratory for Laser Energetics, University of Rochester, 250 East River Road, Rochester New York 14623, USA*
[2)]*Department of Electrical and Computer Engineering University of Alberta, 9211 116th St. NW, Edmonton, AB T6G 1H9, Canada*

(Dated: 5 June 2019)

Absolute instability thresholds for stimulated Raman scattering and two-plasmon decay driven by a broadband laser pulse are evaluated numerically. The scalings of the calculated thresholds with density scale length, temperature, and central wavelength are qualitatively similar to existing analytic results. The threshold values, however, exhibit significant quantitative differences. Comparisons between thresholds calculated for various broadband power spectra indicate a universal scaling of the threshold intensity with laser coherence time (τ_c). For SRS $I_{\text{thr}} \propto \tau_c^{-1/3}$, and for TPD $I_{\text{thr}} \propto \tau_c^{-1/2}$.

I. INTRODUCTION

In direct-drive inertial confinement fusion (ICF), a millimeter-scale spherical capsule is uniformly illuminated by symmetrically oriented laser beams.[1,2] The lasers ablate the outer layer of the capsule, which generates pressure to implode the fuel. The primary mechanism by which laser energy is converted into thermal energy in the ablator is through electron–ion collisional absorption, but a number of parametric instabilities can also occur when the lasers interact with the plasma corona of the imploding capsule, many of which can adversely affect the quality of the implosion.

Of particular importance are the stimulated Raman scattering (SRS) and two-plasmon decay (TPD) instabilities, which correspond to the decay of an incident electromagnetic wave into an electromagnetic wave and an electron plasma wave (EPW) or into two EPWs, respectively.[3,4] The resulting high-phase-velocity EPWs can accelerate electrons to high energies.[5] These energetic electrons can deposit their energy in the cold fuel, reducing the compressibility of the capsule.[1]

It has long been known that introducing bandwidth into the drive lasers reduces the homogeneous growth rate for these parametric instabilities,[6,7] and it has been shown analytically that bandwidth can increase the thresholds for absolute SRS and TPD.[8] However, there are no existing lasers with sufficient energy and bandwidth to suppress SRS or TPD in ICF experiments (typical ICF lasers have relative bandwidths of $\Delta\omega/\omega_0 \lesssim 0.1\%$). Optical parametric amplification of a broadband seed beam using a high-energy monochromatic pump beam provides a potential path toward high-energy broadband lasers ($\Delta\omega/\omega_0 > 1\%$).[9] Stimulated rotational Raman scattering has also been recently shown to provide a promising path toward increasing the bandwidth of high-energy lasers.[10]

This article presents a numerical study of absolute instability thresholds for SRS and TPD using a broadband pump beam. The calculations suggest that the absolute thresholds can be increased significantly with $\sim 1\%$ bandwidth at ICF-relevant conditions. Several different field spectra are considered, and it is found that the coherence time of the laser is the predominant factor in determining the effectiveness of a given pump spectrum. The calculated thresholds are compared to existing analytic formulas. Although there are significant quantitative differences, the calculated thresholds have many qualitative similarities to the analytic predictions, including modification of the threshold scalings (relative to the monochromatic scalings) with respect to density scalelength, temperature, and central wavelength.

Section II of this paper presents the current study in the context of previous work. Section III describes the primary simulation tool used in this study, along with the relevant input parameters used in the simulations. Sections IV and V give the results of the SRS and TPD threshold calculations. Section VI discusses the threshold scalings and gives approximate formulas for the thresholds. Section VII summarizes the results.

II. RELATION TO PREVIOUS WORK

Early work on suppressing parametric instabilities with laser bandwidth focused primarily on homogeneous growth rates. It was shown that for $\Delta\omega \gg \gamma_0$, the homogeneous growth rate was reduced by a factor of $\gamma_0/\Delta\omega$, where $\Delta\omega$ is the laser bandwidth and γ_0 is the homogeneous growth rate.[6,7,11] This scaling was verified experimentally for the parametric-decay instability in a gas discharge plasma.[12] Particle-in-cell (PIC) simulations that were used to study 1-D SRS found qualitative agreement with the analytic result for the homogeneous growth rate.[13–15]

In inhomogeneous plasmas, driven daughter waves with a given frequency and wavenumber propagate out of the resonant region, which leads to convective saturation and finite amplification across the resonant region.[4,16] Guzdar *et al.*[17] showed both analytically and numerically that the convective amplification due to SRS is insensitive to bandwidth because the bandwidth weakens the local growth but broadens the resonance region. However, bandwidth may be helpful in reducing the convective gain amplification that can result from laser speckle and self-focusing.[18] Experiments have shown that $\sim 0.1\%$ bandwidth is sufficient to suppress self-focusing related gain amplification of SRS and TPD, although that was not enough bandwidth to suppress the gain amplification caused by beam speckle.[19,20]

If the pump is sufficiently strong, absolute instability can

occur where the instability grows faster than energy advects out of the resonant region, resulting in temporal growth at a fixed point in space. For TPD and SRS backscatter, absolute instability occurs near quarter-critical densities, where one of the daughter waves has a group velocity near zero.[21–24] Guzdar's model does not apply to the absolute forms of the instabilities because it relies on the WKB approximation, which is invalid for the wave with vanishing group velocity. Lu[8] treated the cases of absolute TPD and SRS with a single broadband pump analytically and found that bandwidth increases the instability thresholds. The main result presented here is the numerical evaluation of the absolute thresholds for SRS and TPD. While the numerical threshold scalings exhibit a number of qualitative features consistent with Lu's predictions, the quantitative thresholds differ significantly.

III. *LPSE*

Most of the simulations discussed here are from the laser-plasma simulation environment (*LPSE*) code.[25,26] *LPSE* solves a set of up to four wave equations for the pump laser light, Raman-scattered light, EPWs, and ion-acoustic waves that are coupled through a linearized plasma response. *LPSE* was previously used in studies using temporal incoherence to suppress cross-beam energy transfer,[27] nonlinear resonance absorption,[28] and TPD.[29] Here, *LPSE* was used to solve the following two equations for the time-enveloped electric fields of Raman-scattered light and EPWs:

$$\left[2i\omega_1\partial_t - c^2(\nabla^2 - \nabla\nabla\cdot) + \omega_1^2\varepsilon(\omega_1;x)\right]\mathbf{E}_1 = -\frac{e\omega_1}{2m_e\omega_0}\frac{n_b(x)}{n_0}\mathbf{E}_0\nabla\cdot\mathbf{E}_h^*. \tag{1}$$

$$\nabla\cdot\left[i\left(\frac{\partial}{\partial t} + \nu_e\circ\right) + \frac{3v_{te}^2}{2\omega_{p0}}\nabla^2 + \frac{\omega_{p0}}{2}\left(1 - \frac{n_b(x)}{n_0}\right)\right]\mathbf{E}_h = S_{\{\mathrm{srs,tpd}\}} + S_h, \tag{2}$$

where $S_{\{\mathrm{srs,tpd}\}}$ is the source term for SRS or TPD,

$$S_{\mathrm{srs}} \equiv \frac{e\omega_{p0}}{4m_e\omega_0\omega_1}\frac{n_b(x)}{n_0}\nabla^2(\mathbf{E}_0\cdot\mathbf{E}_1^*),$$

$$S_{\mathrm{tpd}} \equiv \frac{e}{8\omega_{p0}m_e}\frac{n_b(x)}{n_0}\nabla\cdot[\nabla(\mathbf{E}_0\cdot\mathbf{E}_h^*) - \mathbf{E}_0\nabla\cdot\mathbf{E}_h^*]\,e^{-i(\omega_0-2\omega_{p0})t},$$

only one of which was used depending on the type of simulation. ω_0, $\omega_{p0} = \sqrt{4\pi e^2 n_0/m_e}$, and $\omega_1 = \omega_0 - \omega_{p0}$ are the envelope frequency of the pump light, EPWs, and Raman light, respectively. $\mathbf{E}_0$, $\mathbf{E}_h$, and $\mathbf{E}_1$ are the corresponding electric fields; c is the speed of light; $v_{te} = \sqrt{k_B T_e/m_e}$ is the electron thermal velocity (k_B is Boltzmann's constant); T_e and m_e are the electron temperature and mass; and e is the magnitude of the electron charge. $n_b(x)$ is the background electron density; $\omega_{pe}(x) = \sqrt{4\pi e^2 n_b(x)/m_e}$ is the plasma frequency; and $\varepsilon(\omega_i;x) = 1 - \omega_{pe}^2(x)/\omega_i^2$ is the permittivity. S_h represents a time-random-phase Cerenkov noise source that provides a seed for instability growth. $\nu_e\circ$ is a phenomenological operator (applied in k-space) corresponding to Landau damping. The physical electric fields are $\tilde{\mathbf{E}}_j = \mathrm{Re}\,[\mathbf{E}_j(\mathbf{x},t)\exp(-i\omega_j t)]$ and $\tilde{\mathbf{E}}_h = \mathrm{Re}\,[\mathbf{E}_h(\mathbf{x},t)\exp(-i\omega_{p0}t)]$. In the TPD simulations, only the EPW equation was used ($\mathbf{E}_1 = 0$).

The enveloped field of the drive laser was an applied field of the form

$$\mathbf{E}_0 = \hat{y}\sum_{j=1}^{N_\omega} A_j e^{i(k_j x - \delta\omega_j t + \varphi_j)}, \tag{3}$$

where $N_\omega = 200$ is the number of discrete lines used to approximate continuous power spectra (see Appendix B for a discussion of approximating continuous power spectra with discrete spectral lines); $\delta\omega_j = \omega_j - \omega_0$ is the difference between the frequency of the j^{th} plane wave and the envelope; $k_j = \frac{1}{c}\sqrt{(\omega_0 + \delta\omega_j)^2 - \omega_{p0}^2}$ is the wavenumber; and φ_j is a constant phase offset. The $\delta\omega_j$ were randomly taken from a uniform distribution out to 4% of the peak of the power spectrum, and the φ_j were randomly selected from a uniform distribution over $(0, 2\pi)$. The amplitude of the j^{th} frequency component was

$$A_j = \varepsilon^{-1/4}(\omega_0;x)\sqrt{\frac{8\pi h_\omega I(\delta\omega_j)}{c}},$$

where h_ω is the average spacing between spectral lines, and $I(\omega)$ is the power spectrum of the pump beam. Three different power spectra were used:

$$\begin{aligned}
&\text{Lorentzian:} && I(\omega) = \frac{I_0}{\pi}\frac{\Delta\omega/2}{\omega^2 + (\Delta\omega/2)^2},\\
&\text{Gaussian:} && I(\omega) = I_0\frac{2\ln(2)}{\Delta\omega\sqrt{\pi}}\exp\left[-4\ln(2)\left(\frac{\omega}{\Delta\omega}\right)^2\right],\\
&\text{Flat:} && I(\omega) = \frac{I_0}{\Delta\omega}\mathrm{rect}\left(\frac{\omega}{\Delta\omega}\right),
\end{aligned} \tag{4}$$

where $\mathrm{rect}(x) = 1$, if $|x| < \frac{1}{2}$, and 0 otherwise. I_0 is the time-averaged intensity, and $\Delta\omega$ is the full width at half maximum (FWHM) of the power spectrum.

Another metric that will be used to compare different power spectra is the coherence time:

$$\tau_c \equiv \int_{-\infty}^{\infty} |g(\tau)|^2 d\tau, \tag{5}$$

where

$$g(\tau) \equiv \frac{\langle E_0^*(t)E_0(t+\tau)\rangle}{\langle |E_0(t)|^2\rangle} \tag{6}$$

is the correlation function [the spatial arguments have been suppressed in Eq. 6 because $g(\tau)$ is constant in space]. Using the Wiener-Khinchin theorem, which states that the correlation function and the power spectrum of a wide-sense stationary random process form a Fourier transform pair, gives

$\tau_c = 2/\Delta\omega$, $\sqrt{8\pi\ln(2)}/\Delta\omega$, and $2\pi/\Delta\omega$ for Lorentzian, Gaussian, and flat spectra, respectively.[30]

One other bandwidth model that was used is referred to as a Kubo-Anderson process (KAP), which was used extensively in early studies on using temporal incoherence to suppress laser-plasma instabilities because of its convenience for analytical derivations.[6,7] A laser with KAP bandwidth has a constant amplitude and frequency, but the phase jumps randomly at Poisson distributed intervals with mean jump time τ_c. The amplitude of the phase jumps are uniformly randomly distributed over $(0, 2\pi)$. For a time-enveloped KAP laser, $g(\tau) = e^{-|\tau|/\tau_c}$, which is simply the probability that no phase jump occurs in the interval $[t, t+\tau]$. Again using the Wiener-Khinchin theorem, the power spectrum of a laser with KAP bandwidth is

$$I(\omega) = \frac{I_0}{2\pi}\int_{-\infty}^{\infty} g(\tau)e^{i\omega\tau}d\tau = \frac{I_0}{\pi}\frac{1/\tau_c}{\omega^2 + (1/\tau_c)^2},$$

which shows that KAP and Lorentzian bandwidth have the same power spectrum, and the FWHM of the KAP spectrum is also $\Delta\omega = 2/\tau_c$. Despite having a Lorentzian power spectrum, a beam with KAP bandwidth has very different time-dependent fields than a beam that has randomly chosen phases for the various frequency components. Specifically, the complex envelope of the beam with Lorentzian bandwidth has significant amplitude modulation while the KAP beam has $|\mathbf{E}_0| =$ constant. Note that $\Delta\omega$ was chosen as the FWHM of the power spectrum to be consistent with the optics literature,[30] but this makes $\Delta\omega$ twice as large as the definition typically used in the laser-plasma interactions literature for KAP bandwidth ($\Delta\omega = 1/\tau_c$).

The *LPSE* simulations had a linear density profile from $n_b/n_c = 0.18$ to 0.30 with $n_0/n_c = 0.24$ and a grid resolution of 14 cells per pump wavelength (in vacuum) along each dimension [$n_c = \omega_0^2 m_e/(4\pi e^2)$]. Unless otherwise specified, the simulations had $T_e = 2$ keV, $\lambda_0 = 2\pi c/\omega_0 = 0.351$ μm, and a 100-μm grid along the longitudinal dimension (parallel to the density gradient), which corresponds to a density scalelength of $L_n = 208$ μm. These baseline plasma conditions were chosen because they are similar to the plasma conditions in direct-drive ICF experiments on the OMEGA laser.[31] The SRS simulations were 1-D with absorbing boundaries. Note that because the SRS simulations were 1-D and $\mathbf{E}_0(\mathbf{x}) = \hat{y}E_0(x)$, $\mathbf{E}_1(\mathbf{x})$ must be purely transverse with $\mathbf{E}_1(\mathbf{x}) = \hat{y}E_1(x)$, which implies that the $\nabla^2 - \nabla\nabla\cdot$ operator in Eq. 1 simplifies to ∂_x^2. The TPD simulations were 2-D, p-polarized with absorbing longitudinal boundaries and periodic transverse boundaries. The nominal transverse width of the 2-D simulations was 10 μm. In the calculations of the TPD threshold scaling with central wavelength [Fig. 5(b)], the width was scaled as $\lambda_0^{2/3}$ to match the simulations' ability to resolve the transverse component of the dominant absolute mode with the analytic result for a monochromatic pump.[21]

The simulations included Landau damping, but the Landau-damping rate was effectively 0 for the dominant absolute modes observed in the simulations: the fastest-growing electrostatic modes typically had $k\lambda_{De} \sim 0.11$, significantly less than the $k\lambda_{De} \gtrsim 0.25$ required to have significant Landau damping ($\lambda_{De} \equiv v_{te}/\omega_{pe}$).

IV. STIMULATED RAMAN SCATTERING

Figure 1 shows absolute instability thresholds for SRS as a function of pump bandwidth for Gaussian, Lorentzian, and flat power spectra from simulations with (a) $L_n = 208$ μm and (b) $L_n = 416$ μm. The thresholds are normalized to the analytic threshold for absolute backscatter of a monochromatic pump at $n_c/4$[24]

$$\left(\frac{v_{os}}{c}\right)^2_{thr,srs} = \frac{2^{4/3}}{3}\left(\frac{c}{\omega_0 L_n}\right)^{4/3}, \tag{7}$$

where $v_{os} = e/(m_e\omega_0)\sqrt{8\pi I/c}\,\varepsilon^{-1/4}(\omega_0; x)$ is the electron oscillation velocity [$\varepsilon(\omega_0; x) = 3/4$ was used here because the absolute instability occurs near $n_c/4$]. In terms of laser intensity,

$$I_{thr,srs} = \frac{2^{1/3}}{\sqrt{3}}\left(\frac{c}{\omega_0 L_n}\right)^{4/3}\frac{m_e^2\omega_0^2 c^3}{8\pi e^2}. \tag{8}$$

Equation (8) is in cgs units, so the right-hand side must be multiplied by 10^{-7} to put the threshold in W/cm^2.

The error bars on the thresholds correspond to the standard deviation from four-run ensembles varying the random-number-generator seed for the frequency components ($\delta\omega_j$) and phases (φ_j) of the beams as well as the electrostatic noise (S_h). In addition, there is systematic uncertainty because the technique that was used to calculate the thresholds converges asymptotically in the limit of infinite run time. For the run times used here, the calculated thresholds were systematically high by $\sim 10\%$. The technique and the associated convergence are discussed in Appendix A.

The bandwidth required to suppress absolute SRS is consistent with the expectation that significant instability suppression requires $\gamma_0\tau_c \ll 1$, where $\gamma_0 \approx k_0 v_{os}/4$ for SRS backscatter at quarter-critical densities.[3] For example, for Lorentzian bandwidth of $\Delta\omega/\omega_0 = 1\%$ and $L_n = 208$ μm, $I_{thr} = 4.1\times10^{14}$ W/cm^2 $\Longrightarrow \gamma_0\tau_c = 0.25$. For $L_n = 416$ μm, $I_{thr} = 2.0\times10^{14}$ W/cm^2 $\Longrightarrow \gamma_0\tau_c = 0.18$.

In addition to the *LPSE* results, Fig. 1 shows SRS thresholds from the 1-D Vlasov-Maxwell code *ARGOS*. The Vlasov simulations were performed primarily as a check on the *LPSE* results because of the poor quantitative agreement with the analytic thresholds, which will be discussed in the following section. *ARGOS* solved the same equations (the 1-D Vlasov equation coupled to Maxwell's equations) and used similar boundary conditions to the *ELVIS* code,[32] but we used the Yee algorithm for the electromagnetic solver[33] and the piecewise parabolic method for the advection.[34] The Poisson equation was solved using the pseudospectral method. *LPSE* and *ARGOS* give the same result to within error for nearly all of the cases. The difference in simulation time between *ARGOS* and *LPSE* highlights the advantage of a fluid-based solver. The *LPSE* calculations shown in Fig. 1(a) took 0.024 CPU hours

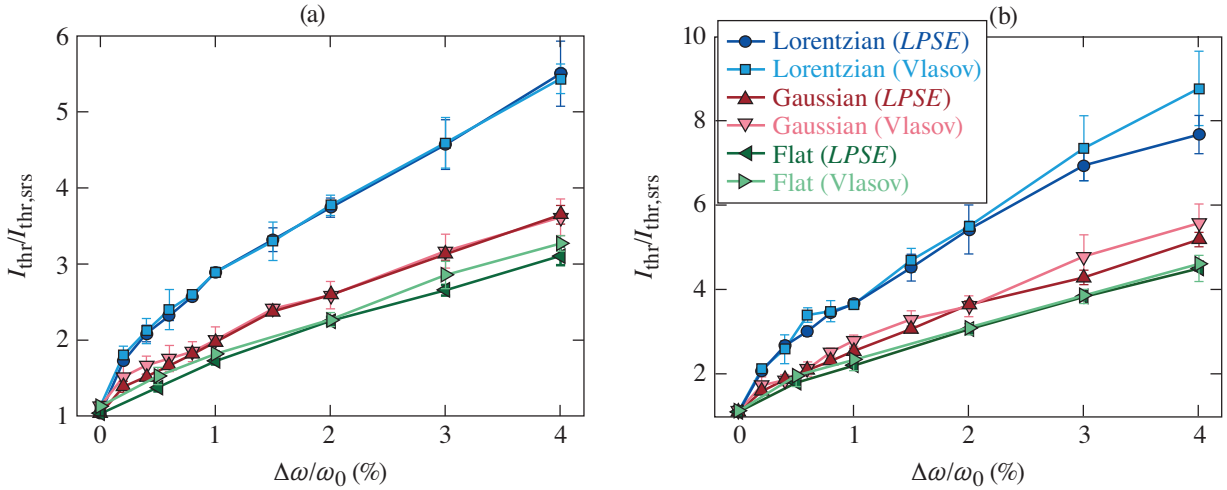

FIG. 1. Absolute SRS thresholds for different field spectra normalized to the monochromatic threshold for (a) $L_n = 208\ \mu$m and (b) $L_n = 416\ \mu$m. The *LPSE* results are shown with blue circles (Lorentzian), red upward-pointing triangles (Gaussian), and green left-pointing triangles (flat). Results from Vlasov simulations are shown with light-blue squares (Lorentzian), pink downward-pointing triangles (Gaussian), and light-green right-pointing triangles (flat).

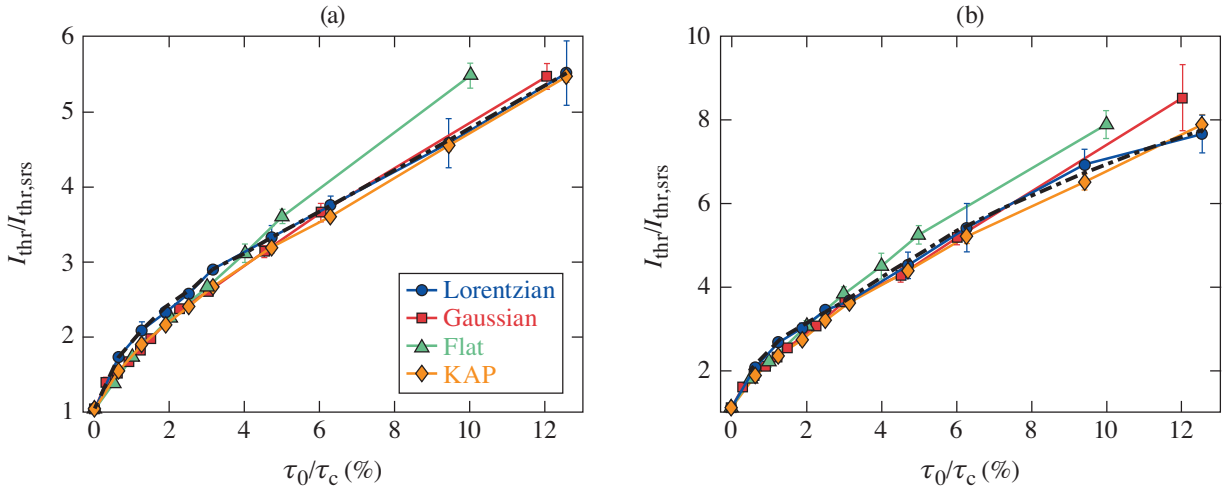

FIG. 2. Absolute SRS thresholds from *LPSE* simulations plotted in terms of the laser period over the coherence time for (a) $L_n = 208\ \mu$m and (b) $L_n = 416\ \mu$m. The various field spectra are represented by blue circles (Lorentzian), red squares (Gaussian), green triangles (flat), and orange diamonds (KAP). The dashed curves correspond to power law fits to the Lorentzian results over $0.3\% \leq \tau_0/\tau_c \leq 3.14\%$, and the dashed-dotted curves correspond to power law fits for $\tau_0/\tau_c \geq 3.14\%$.

per ps of simulation time whereas the *ARGOS* calculations took 5.5 CPU hours per ps.

The large differences in threshold between the various bandwidth spectra in Fig. 1 can be eliminated by plotting the thresholds in terms of the coherence time instead of $\Delta\omega$ (the FWHM of the power spectrum). Figure 2 shows the SRS thresholds from the *LPSE* calculations shown in Fig. 1 plotted as a function of the laser period [$\tau_0 = \omega_0/(2\pi)$] over the coherence time. In addition to the three power spectra shown in Fig. 1, Fig. 2 shows the threshold for KAP bandwidth. Despite being the only field spectrum that does not have amplitude modulation in the time domain, KAP bandwidth results in nearly the same thresholds as the other spectra, which indicates that amplitude modulation does not significantly impact the absolute threshold. The fact that the coherence time provides a universal scaling for the instability thresholds can be traced back to the early analytic work by Thomson.[6] The coherence time is defined in terms of the autocorrelation of the laser field, which also appears in the analytic homogeneous growth rate.

Note that coherence time is expected to be a good metric for instability suppression only for pump lasers with continuous broadband spectra and random spectral phases. For example, a power spectrum consisting of a small number of discrete lines can still provide significant instability suppression even though τ_c is infinite,[29] and a chirped laser pulse is not expected

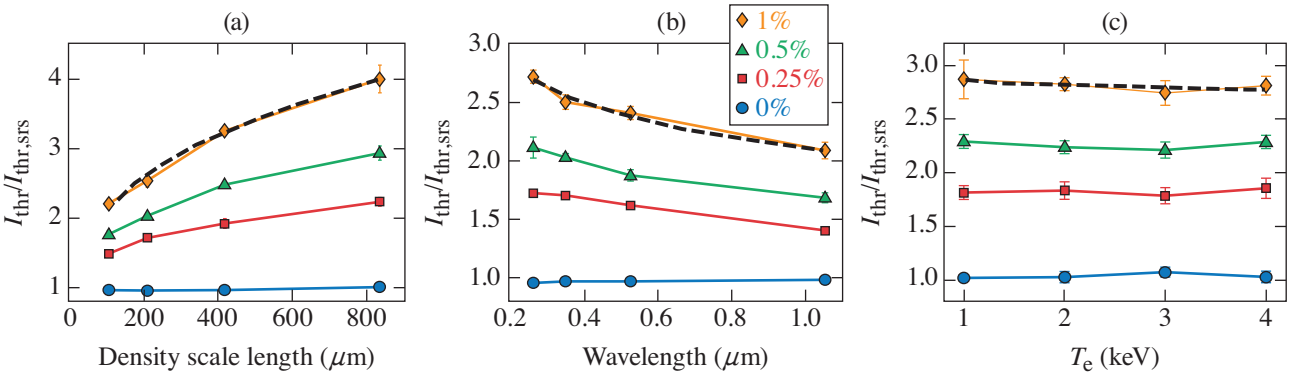

FIG. 3. Absolute SRS thresholds with Lorentzian bandwidth as a function of (a) density scalelength, (b) central wavelength, and (c) electron temperature. The thresholds are normalized to the analytic result for a monochromatic pump beam. Threshold curves are shown for $\Delta\omega/\omega_0 = 0\%$ (blue circles), $\Delta\omega/\omega_0 = 0.25\%$ (red squares), $\Delta\omega/\omega_0 = 0.5\%$ (green triangles), and $\Delta\omega/\omega_0 = 1\%$ (orange diamonds). The black dashed curves correspond to power-law fits.

to provide the same degree of instability suppression as its random-spectral-phase counterpart.

A. SRS Threshold Scalings

For practical applications, it would be beneficial to have universal scaling laws for the absolute instability thresholds when using a temporally incoherent pump. The similarity in thresholds between the various power spectra in Fig. 2 suggests that common scaling laws can be applied to all of the spectra by converting from $\Delta\omega$ to τ_c. To obtain scaling laws, the calculated thresholds were fit to power laws. As suggested by Lu,[8] two separate regions were used: large and small bandwidth. For $0.003 \le \tau_0/\tau_c \le 0.0314$, the curves were fit to $I_{thr}/I_{thr,srs} = a(\tau_0/\tau_c)^n$, where a and n are the fitting parameters. For $\tau_0/\tau_c \ge 0.0314$, the curves were fit to $I_{thr}/I_{thr,srs} = a(\tau_0/\tau_c)^n + b$, where a, b, and n are the fitting parameters. A constant offset was included in the fitting for large $\Delta\omega$ because the threshold curve can smoothly transition from $n < 1$ at small $\Delta\omega$ to $n = 1$ at large $\Delta\omega$ only if the linear part of the curve crosses the ordinate above the origin. For the 208-μm-scalelength simulations [Fig. 2(a)], the mean and standard deviations of the fits to the four different field spectra gave $n = 0.34 \pm 0.03$ ($a = 9.0 \pm 0.6$) for small $\Delta\omega$ and $n = 0.87 \pm 0.17$ ($a = 27 \pm 5$, $b = 1.3 \pm 0.8$) for large $\Delta\omega$. The corresponding results for the 416-μm-scalelength simulations [Fig. 2(b)] are $n = 0.41 \pm 0.04$ ($a = 15 \pm 2$) for small $\Delta\omega$ and $n = 0.71 \pm 0.37$ ($a = 40 \pm 22$, $b = 0 \pm 3$) for large $\Delta\omega$.

A surprising aspect of using a broadband pump to suppress absolute SRS and TPD is that not only does it introduce a $\Delta\omega$ dependence in the threshold, but it modifies the dependence on the other parameters appearing in the monochromatic threshold scalings: L_n, T_e, and λ_0. Accordingly, the scaling laws must undergo a transition from the monochromatic scalings to the broadband scalings. This transition is shown in Fig. 3, where *LPSE*-calculated thresholds are shown as a function of (a) scalelength, (b) central wavelength, and (c) temperature using Lorentzian bandwidth with $\Delta\omega/\omega_0 = 0\%$, 0.25%, 0.5%, and 1%. The curves are normalized to the analytic monochromatic threshold [Eq. (8)], which makes it easy to tell if the introduction of temporal incoherence has modified the threshold scaling; an unmodified threshold scaling corresponds to a constant threshold in Fig. 3. For example, the temperature scaling does not change because all of the curves are constant in Fig. 3(c), but the scalelength [Fig. 3(a)] and central wavelength [Fig. 3(b)] scalings do change. Power-law fits [$I_{thr}(x)/I_{thr,srs} = ax^n$] to the curves in Fig. 3 corresponding to $\Delta\omega/\omega_0 = 1\%$ are shown as dashed black curves. The fits give $n_{L_n} = 0.30$, $n_{\lambda_0} = -0.18$, and $n_{T_e} = -0.02$ for the density scalelength, central wavelength, and temperature scalings, respectively.

B. Comparison with the analytic threshold

The power-law fits shown in Figs. 2 and 3 can be compared to the analytic result given by Lu[8]:

$$\left(\frac{v_{os}}{c}\right)^2_{Lu,srs} = 3^{1/12}2^{7/8}\frac{1}{k_0 L_n}\left(\frac{\tau_0}{2\pi\tau_c}\right)^{1/3} \qquad (\beta < 1), \quad (9a)$$

$$\left(\frac{v_{os}}{c}\right)^2_{Lu,srs} = \frac{1}{3}\frac{1}{k_0 L_n}\frac{\tau_0}{2\pi\tau_c} \qquad (\beta > 1), \quad (9b)$$

where

$$\beta \equiv 2^{2/3}3^{-1/3}\left(\frac{v_{os}}{c}\right)^2 k_0 L_n \left(\frac{\tau_0}{2\pi\tau_c}\right)^{1/3}, \qquad (10)$$

where the replacement $(\Delta\omega/\omega_0)_{Lu} \to \Delta\omega/2\omega_0 \to \tau_0/2\pi\tau_c$ has been made to account for the different definitions of $\Delta\omega$ and the fact that Lu assumed KAP bandwidth. The first qualitative feature that appears in both the numerical result and Lu's result is the transition from a 1/3 power-law scaling at small bandwidth to a linear scaling at large bandwidth. To compare the other scaling parameters, we take the ratio of Eq. (9a) to

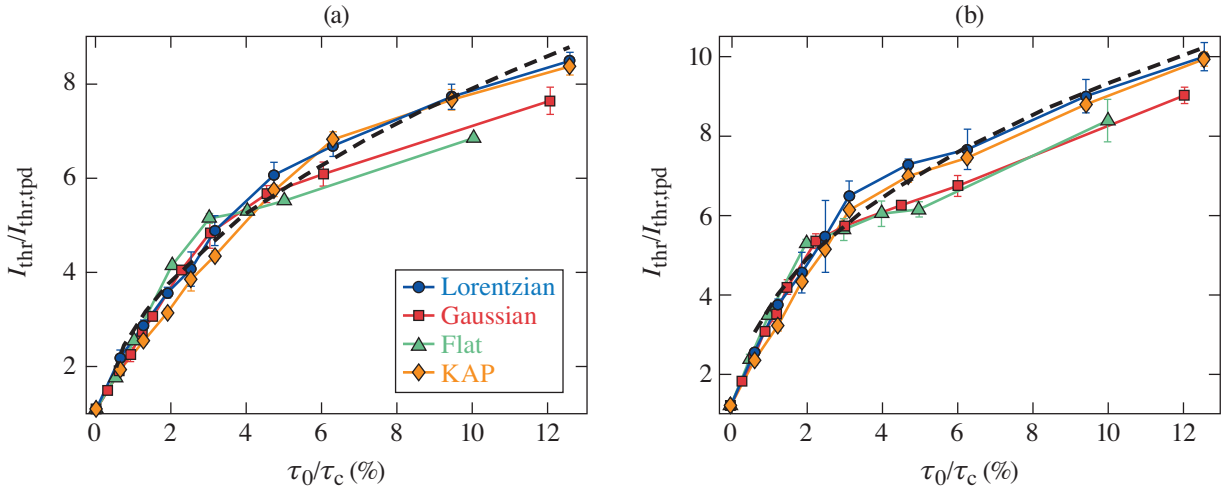

FIG. 4. Absolute TPD thresholds from *LPSE* simulations plotted in terms of the laser period over the coherence time for (a) $L_n = 208$ μm and (b) $L_n = 416$ μm. The various field spectra are represented by blue circles (Lorentzian), red squares (Gaussian), green triangles (flat), and orange diamonds (KAP). The black dashed curves correspond to a power-law fit to the Lorentzian results for $\tau_0/\tau_c \geq 0.3\%$.

the monochromatic threshold [Eq. (7)]:

$$\frac{I_{\mathrm{Lu,srs}}}{I_{\mathrm{thr,srs}}} \propto \left(\frac{L_n}{\lambda_0}\right)^{1/3} \left(\frac{\tau_0}{\tau_c}\right)^{1/3}. \tag{11}$$

This gives $n_{\mathrm{Lu},L_n} = 1/3$, $n_{\mathrm{Lu},\lambda_0} = -1/3$, and $n_{\mathrm{Lu},T_e} = 0$ for the density scalelength, central wavelength, and temperature scalings, respectively, which are all in reasonable agreement with the calculated scalings. The (unnormalized) power-law scalings from the monochromatic threshold, the Lu threshold, and the fits to the numerical thresholds are summarized in Table I.

	$I_{\mathrm{thr,srs}}$	$I_{\mathrm{Lu,srs}}$	I_{thr}
$\Delta\omega$ (small $\Delta\omega$)	N/A	0.33	0.38
$\Delta\omega$ (large $\Delta\omega$)	N/A	1	0.79
L_n	-1.33	-1	-1.03
λ_0	-0.66	-1	-0.84
T_e	0	0	-0.02

TABLE I. SRS absolute threshold power-law dependence on $\Delta\omega$, L_n, λ_0, and T_e from the analytic monochromatic result ($I_{\mathrm{thr,srs}}$), the analytic result with bandwidth ($I_{\mathrm{Lu,srs}}$), and the fits to the *LPSE* results (I_{thr}). The $\Delta\omega$ scalings are averages over all eight curves in Fig. 3.

Despite the good qualitative agreement, there are significant quantitative differences between the numerically evaluated thresholds and the Lu results. Equation (9a) predicts thresholds that are $\sim 3\times$ larger than the calculated thresholds. Additionally, the transition from a $1/3$ power-law scaling with τ_0/τ_c to a linear scaling occurs well below $\beta = 1$. By plugging Eq. (9) into Eq. (10), it is straightforward to show that Eq. (9) does not correspond to a continuous curve at $\beta = 1$, and that coming from below, $\beta < 1$ until $\tau_0/\tau_c = 1.91$ ($\Delta\omega/\omega_0 = 61\%$ for KAP bandwidth), which is well above the $\tau_0/\tau_c = 0.0314$ that was used as the transition point in the fits.

V. TWO-PLASMON DECAY

Figure 4 shows *LPSE*-simulated TPD thresholds for normally incident pump beams with Lorentzian, Gaussian, flat, and KAP bandwidth. The thresholds are normalized to the monochromatic analytic result[21]

$$\left(\frac{v_{os}}{c}\right)^2_{\mathrm{thr,tpd}} = \frac{\alpha}{k_0 L_n}\left(\frac{v_{te}}{c}\right)^2, \tag{12}$$

where $\alpha \equiv 16.536$. In terms of laser intensity (cgs units)

$$I_{\mathrm{thr,tpd}} = \frac{\alpha c^4 m_e^2 \omega_0}{8\pi e^2 L_n}\frac{v_{te}^2}{c^2}. \tag{13}$$

Similar to the SRS case, all of the different field spectra have similar threshold scalings when plotted in terms of τ_0/τ_c, and significant instability suppression requires $\gamma_0\tau_c \ll 1$, where $\gamma_0 \approx k_0 v_{os}/4$. For Lorentzian bandwidth at $\Delta\omega/\omega_0 = 1\%$ and $L_n = 208$ μm, $I_{\mathrm{thr}} = 8.3\times10^{14}$ W/cm^2 $\Longrightarrow$ $\gamma_0\tau_c = 0.37$. For $L_n = 416$ μm, $I_{\mathrm{thr}} = 6.3\times10^{14}$ W/cm^2 $\Longrightarrow$ $\gamma_0\tau_c = 0.32$.

A. TPD threshold scalings

Again motivated by Lu's results,[8] only a single power law $[I_{\mathrm{thr}}/I_{\mathrm{thr,tpd}} = a(\tau_0/\tau_c)^n]$ was fit to the threshold curves in Fig. 4 over the entire bandwidth range (excluding the points at $\tau_0/\tau_c = 0$). The mean and standard deviation of the fits gave $n = 0.44\pm0.05$ ($a = 21\pm3$) and $n = 0.40\pm0.03$ ($a = 22\pm3$) for the 208- and 416-μm- scalelength simulations, respectively. Although not shown here, in calculations out to larger bandwidths, the TPD threshold appears to transition to a linear dependence on τ_0/τ_c, like it does for SRS.

Following the same procedure as for SRS, we obtained threshold scalings with L_n, λ_0, and T_e. Figure 5 shows the

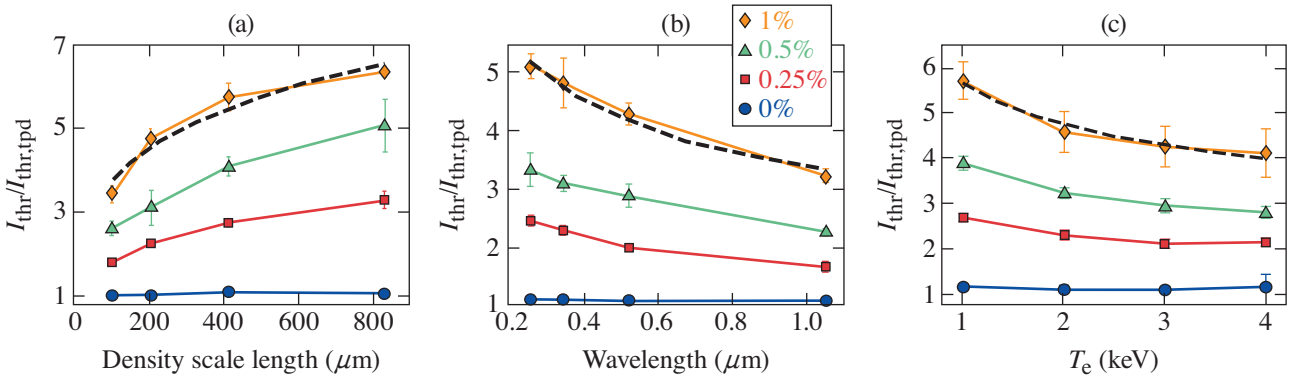

FIG. 5. Absolute TPD thresholds with Lorentzian bandwidth as a function of (a) density scalelength, (b) central wavelength, and (c) electron temperature. The thresholds are normalized to the analytic result for a monochromatic pump beam. Threshold curves are shown for $\Delta\omega/\omega_0 = 0\%$ (blue circles), $\Delta\omega/\omega_0 = 0.25\%$ (red squares), $\Delta\omega/\omega_0 = 0.5\%$ (green triangles), and $\Delta\omega/\omega_0 = 1\%$ (orange diamonds). The black dashed curves correspond to power-law fits.

thresholds as functions of scalelength, central wavelength, and temperature for Lorentzian bandwidth and the corresponding power-law fits for $\Delta\omega/\omega_0 = 1\%$. The power-law $[I_{thr}(x)/I_{thr,tpd} = ax^n]$ fits gave $n_{L_n} = 0.27$, $n_{\lambda_0} = -0.32$, and $n_{T_e} = -0.25$.

B. Comparison with the analytic threshold

The Lu result for the TPD threshold is

$$\left(\frac{v_{os}}{c}\right)^2_{Lu,tpd} = 4(2/3)^{1/2}\frac{1}{k_0 L_n}\frac{v_{te}}{c}\left(\frac{\tau_0}{2\pi\tau_c}\right)^{1/2}, \qquad (14)$$

which predicts thresholds that are $\sim 20\times$ smaller than the calculations. Dividing out the monochromatic threshold gives

$$\frac{I_{Lu,tpd}}{I_{thr,tpd}} \propto T_e^{-1/2}\left(\frac{\tau_0}{\tau_c}\right)^{1/2}. \qquad (15)$$

The Lu threshold prediction has a $\Delta\omega$ scaling that is similar to the numerical result, but Eq. (15) suggests that only the temperature scaling should change at large $\Delta\omega$, whereas the threshold scalings with L_n, λ_0, and T_e all changed in the calculated thresholds. The (unnormalized) power-law scalings from the monochromatic threshold, the Lu threshold, and the fits to the numerical thresholds are summarized in Table II.

	$I_{thr,tpd}$	$I_{Lu,tpd}$	I_{thr}
$\Delta\omega$	N/A	0.5	0.42
L_n	-1	-1	-0.73
λ_0	-1	-1	-1.32
T_e	1	0.5	0.75

TABLE II. TPD absolute threshold power law dependence on $\Delta\omega$, L_n, λ_0, and T_e from the analytic monochromatic result ($I_{thr,tpd}$), the analytic result with bandwidth ($I_{Lu,tpd}$), and the fits to the *LPSE* results (I_{thr}). The $\Delta\omega$ scalings are averages over all eight curves in Fig. 5.

VI. DISCUSSION

Although the results in Tables I and II provide a useful guide, many more simulations would be required to obtain scaling laws over a significant fraction of the ($\Delta\omega$, L_n, ω_0, T_e) space that could potentially be accessed experimentally. However, we can give approximate scaling laws for the SRS and TPD thresholds with modest bandwidth:

$$\left(\frac{v_{os}}{c}\right)^2_{\Delta\omega,srs} \approx 0.067\frac{\lambda_0}{L_n}\left(\frac{\tau_0}{\tau_c}\right)^{1/3}, \qquad (16)$$

$$\left(\frac{v_{os}}{c}\right)^2_{\Delta\omega,tpd} \approx 2.1\left(\frac{\lambda_0}{L_n}\right)^{2/3}\left(\frac{v_{te}}{c}\right)^{3/2}\left(\frac{\tau_0}{\tau_c}\right)^{1/2}, \qquad (17)$$

or in terms of laser intensity in units of 10^{14} W/cm^2,

$$I_{14,\Delta\omega,srs} \approx \frac{798}{L_n^{\mu m}\lambda_0^{\mu m}}\left(\frac{\tau_0}{\tau_c}\right)^{1/3}, \qquad (18)$$

$$I_{14,\Delta\omega,tpd} \approx \frac{232(T_e^{keV})^{3/4}}{(L_n^{\mu m})^{2/3}(\lambda_0^{\mu m})^{4/3}}\left(\frac{\tau_0}{\tau_c}\right)^{1/2}, \qquad (19)$$

where $L_n^{\mu m}$ and $\lambda_0^{\mu m}$ are the density scalelength and central wavelength in microns, and T_e^{keV} is the electron temperature in keV.

Note that the powers appearing in Eqs. 16-19 were not derived rigorously but correspond to an educated guess at what the true scaling laws are based on a combination of the simulation results presented here and the analytic results from Lu. The simulated SRS threshold powers were sufficiently close to the Lu result that we assumed the Lu result was correct up to a constant coefficient. The powers appearing in the TPD threshold were chosen based on a combination of the Lu result, the fit results, dimensionality arguments, and symmetry between the SRS and TPD thresholds. In particular, on the basis of the agreement between the simulation results and Lu's results for

the SRS scalings, it was assumed that the TPD threshold also has simple rational powers of its arguments.

Equations (16) and (18) apply only to a pump with modest bandwidth. At large bandwidth, the τ_0/τ_c dependence becomes linear, but the set of simulations presented here is not sufficient to generate a scaling law for where this transition occurs. For the plasma conditions discussed here, Eqs. (16) and (18) are a good approximation out to approximately $\tau_0/\tau_c = 0.04$.

VII. SUMMARY

Absolute instability thresholds and scaling laws for a broadband pump laser were calculated for SRS and TPD. The calculations suggest that $\sim 1\%$ bandwidth would significantly increase the instability thresholds at ICF-relevant conditions. The calculated thresholds were compared to existing analytic results. The numerically evaluated thresholds had qualitative similarities to the analytic results, but significant quantitative differences. Approximate threshold formulas were provided based on the numerical results. In addition to adding a bandwidth-dependent term to the monochromatic threshold scalings, the introduction of laser bandwidth was found to change the threshold scaling with density scalelength, central wavelength, and electron temperature. Comparisons between thresholds calculated for various pump-laser power spectra indicate that coherence time is the dominant factor in determining the effectiveness for instability suppression.

ACKNOWLEDGMENTS

This material is based upon work supported by the Department of Energy National Nuclear Security Administration under Award Number DE-NA0003856, the University of Rochester, and the New York State Energy Research and Development Authority.

This report was prepared as an account of work sponsored by an agency of the U.S. Government. Neither the U.S. Government nor any agency thereof, nor any of their employees, makes any warranty, express or implied, or assumes any legal liability or responsibility for the accuracy, completeness, or usefulness of any information, apparatus, product, or process disclosed, or represents that its use would not infringe privately owned rights. Reference herein to any specific commercial product, process, or service by trade name, trademark, manufacturer, or otherwise does not necessarily constitute or imply its endorsement, recommendation, or favoring by the U.S. Government or any agency thereof. The views and opinions of authors expressed herein do not necessarily state or reflect those of the U.S. Government or any agency thereof.

Appendix A: Determining absolute thresholds

A parametric instability is absolutely unstable if, in the absence of saturation mechanisms, the decay waves grow indefinitely at a fixed point in space. The primary challenge in determining the absolute threshold using a code like *LPSE* is coming up with a criterion for what constitutes absolute instability in a finite simulation time. This is particularly challenging when the pump has bandwidth because the decay waves do not grow at a steady rate, so a long simulation time is required to determine if the instability is growing on average. This results in the requirement that the run time be much greater than the bandwidth cycle time, $2\pi/\Delta\omega$ (e.g., with 0.1% bandwidth, the simulation needs to be much longer than 1.2 ps). Additionally, it is necessary that the instability grows enough to distinguish absolute instability from convective instability. In most of the *LPSE* results presented here, a simulation was deemed to be absolutely unstable if the largest electron density perturbation was at least ten orders of magnitude greater than the noise level after 100 ps. Figure 6 shows the temporal growth of the maximum electrostatic density perturbation in 1-D SRS simulations for a monochromatic pump and a pump

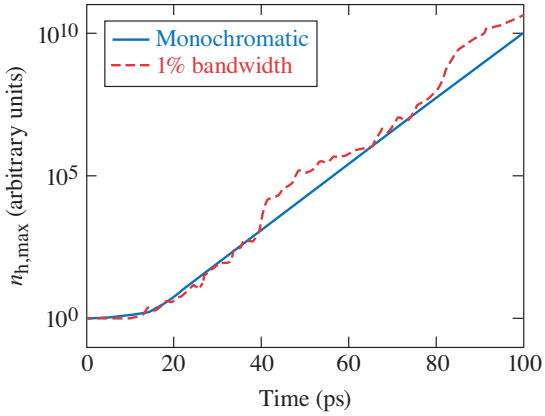

FIG. 6. Temporal growth of largest electron density perturbation in absolute instability threshold calculations of a monochromatic pump (solid blue curve) and a pump with 1% Lorentzian bandwidth (dashed red curve).

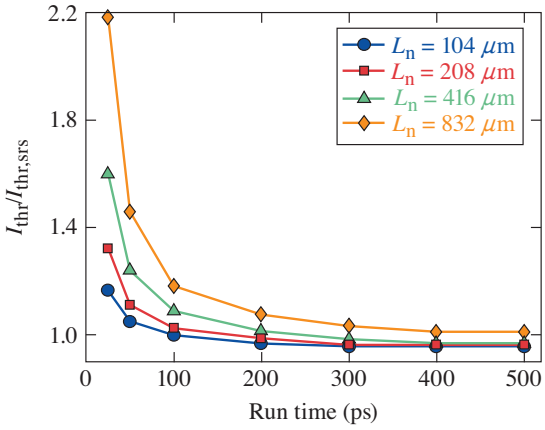

FIG. 7. Absolute SRS thresholds as a function of run time for 104- (blue circles), 208- (red squares), 416- (green triangles), and 832-μm scalelengths (orange diamonds).

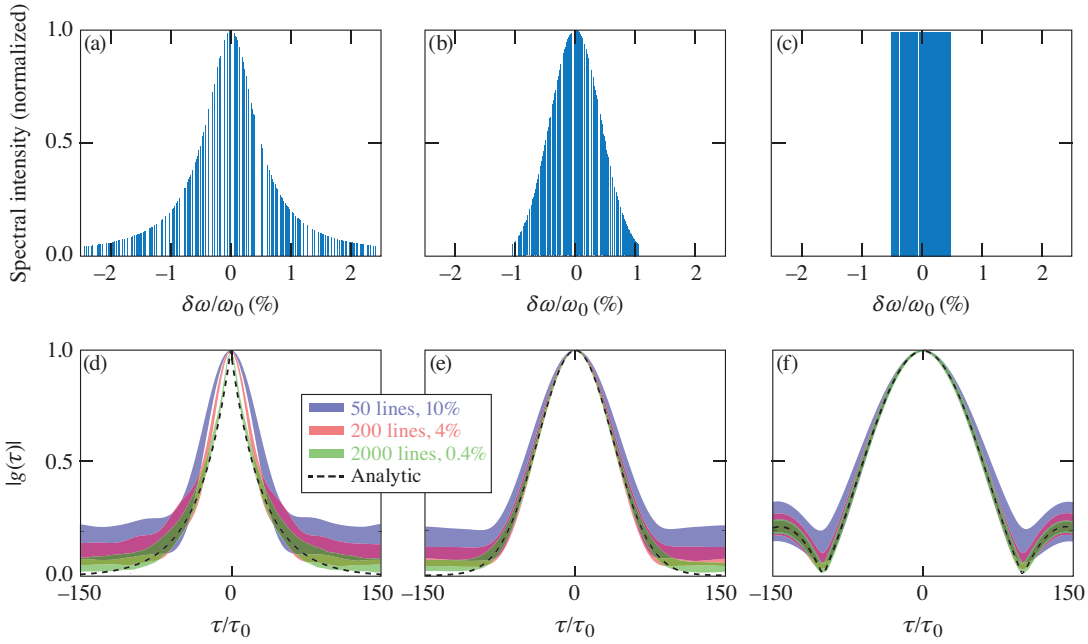

FIG. 8. Sample power spectra and correlation functions for [(a),(d)] Lorentzian, [(b),(e)] Gaussian, and [(c),(f)] flat bandwidth. The sample power spectra have 200 lines going out to 4% of the peak intensity. The correlation functions are evaluated using 50 lines out to 10% of the peak (blue-shaded region), 200 lines out to 4% of the peak (red-shaded region), and 2000 lines out to 0.4% of the peak (green-shaded region). The width of the shaded regions corresponds to the standard deviation from an ensemble of 100 randomly generated spectra. The dashed black curves correspond to the analytic correlation functions.

with 1% Lorentzian bandwidth.

Using the above criteria for absolute instability, the thresholds were determined by iteratively running simulations and adjusting the drive intensity to bound the threshold. Initial bounds on the thresholds were determined by making an initial guess at the threshold and then adjusting the intensity up or down until bounds were established. Then the interval was iteratively divided in half to obtain the desired level of accuracy. The initial intensity step size was set at $1/3$ of the initial guess, which means that once the bounds are established, the uncertainty in the threshold was $1/6$ of the initial guess. Five more iterations were used after bounding the threshold, resulting in an uncertainty of $\frac{1}{6}\left(\frac{1}{2}\right)^5 = 0.52\%$ of the initial guess, which was typically much smaller than the uncertainty associated with the ensemble of bandwidth realizations.

Figure 7 shows monochromatic absolute SRS thresholds as a function of the length of the runs that were used to determine the threshold for grid sizes ranging from 50 to 400 μm (the scalelength was 2.16$\times$ the grid size). The calculated thresholds converge asymptotically with increasing run time, but the longer scalelength simulations converge more slowly (presumably because the absolute thresholds are at lower homogeneous growth rates). Based on the results shown in Fig. 7, we estimate that for the majority of the results presented here, the calculated thresholds are systematically higher than they would have been in the limit of infinite run time by $\sim 6\%$ and $\sim 11\%$ for the $L_n = 208$- and 416-μm simulations, respectively.

To obtain accurate scaling laws from the calculations shown in Figs. 3 and 5, it is important that the monochromatic calculations give nearly constant normalized thresholds because any systematic variations in the monochromatic thresholds would likely imprint on the broadband results. For example, in the simulations where the scalelength was varied, the results from Fig. 7 were used to vary the run time to maintain a relatively constant level of convergence (the actual run times that were used were 200, 300, 400, and 500 ps). The wavelength scaling simulations were all run for 200 ps (rather than the typical 100 ps) to improve the overall convergence because it was not immediately obvious how the convergence would scale with central wavelength. The temperature scalings used the nominal run time because the convergence did not appear to have a systematic dependence on temperature.

The threshold criterion that was used in the *LPSE* simulations could not be used in the Vlasov-Maxwell simulations because they inherently have nonlinear saturation mechanisms that limit the instability growth (e.g., pump depletion, wave breaking, etc.). The Vlasov simulations were deemed to be absolutely unstable if the electron density perturbation began to approach the levels where nonlinear saturation occurs over the course of 40 ps. An imposed noise seed was not required in the Vlasov simulations because the instability grew from the inherent numerical noise that results from initializing the simulations with an inhomogeneous plasma profile (in the absence of imposed noise, $\mathbf{E}_h$ and $\mathbf{E}_1$ would be zero for all time in the *LPSE* simulations, which can readily be verified by looking at Eqs. 1 and 2 with $S_h = 0$).

Appendix B: Approximating power spectra

When approximating a continuous spectrum by a sum of monochromatic plane waves, the simulation results are sensitive to the number of frequencies (N_ω) that are used and where the tails of the spectra are truncated. Figure 8 shows samples of the (a) Lorentzian, (b) Gaussian, and (c) flat power spectra at 1% bandwidth that had 200 lines and extended out to 4% of the peak intensity. A straightforward way to check how well a discrete spectrum approximates a continuous spectrum is to look at the convergence of the correlation function [Eq. (6)]. Numerically evaluated correlation functions are shown in Fig. 8 for (d) Lorentzian, (e) Gaussian, and (f) flat spectra using N_ω =50, 200, and 2000 spectral lines going out to 10%, 4%, and 0.4% of the peak, respectively. Because of the long tails, the Lorentzian power spectrum is the most difficult to approximate, and the discrete case is still visually different from the analytic result with 200 lines (although this degree of difference was found not to have a significant impact on threshold calculations). For the Gaussian and flat spectra, only 50 lines were required to obtain a good approximation to the analytic result.

[1] R. S. Craxton, K. S. Anderson, T. R. Boehly, V. N. Goncharov, D. R. Harding, J. P. Knauer, R. L. McCrory, P. W. McKenty, D. D. Meyerhofer, J. F. Myatt, A. J. Schmitt, J. D. Sethian, R. W. Short, S. Skupsky, W. Theobald, W. L. Kruer, K. Tanaka, R. Betti, T. J. B. Collins, J. A. Delettrez, S. X. Hu, J. A. Marozas, A. V. Maximov, D. T. Michel, P. B. Radha, S. P. Regan, T. C. Sangster, W. Seka, A. A. Solodov, J. M. Soures, C. Stoeckl, and J. D. Zuegel, Phys. Plasmas **22**, 110501 (2015).

[2] S. Atzeni and J. Meyer-ter Vehn, *The Physics of Inertial Fusion: Beam Plasma Interaction, Hydrodynamics, Hot Dense Matter*, International Series of Monographs on Physics (Clarendon, Oxford, 2004).

[3] W. L. Kruer, *The Physics of Laser Plasma Interactions*, Frontiers in Physics, Vol. 73 (Addison-Wesley, Redwood City, CA, 1988).

[4] C. S. Liu and V. K. Tripathi, *Interaction of Electromagnetic Waves with Electron Beams and Plasmas* (World Scientific Publishing Co. Pte. Ltd., Singapore, 1994).

[5] R. Yan, C. Ren, J. Li, A. V. Maximov, W. B. Mori, Z. M. Sheng, and F. S. Tsung, Phys. Rev. Lett. **108**, 175002 (2012).

[6] J. J. Thomson and J. I. Karush, Phys. Fluids **17**, 1608 (1974).

[7] G. Laval, R. Pellat, D. Pesme, A. Ramani, M. N. Rosenbluth, and E. A. Williams, Phys. Fluids **20**, 2049 (1977).

[8] L. Lu, Phys. Fluids B **1**, 1605 (1989).

[9] G. Cerullo and S. D. Silvestri, Rev. Sci. Instrum. **74**, 1 (2003).

[10] J. Weaver, R. Lehmberg, S. Obenschain, D. Kehne, and M. Wolford, Appl. Opt. **56**, 8618 (2017).

[11] D. Pesme, R. L. Berger, E. A. Williams, A. Bourdier, and A. Burtuzzo-Lesne, arXiv , 0710:22195 (2007).

[12] S. P. Obenschain, N. C. Luhmann, and P. T. Greiling, Phys. Rev. Lett. **36**, 1309 (1976).

[13] G. Bonnaud and C. Reisse, Nucl. Fusion **26**, 633 (1986).

[14] Y. Zhao, L. L. Yu, J. Zheng, S. M. Weng, C. Ren, C. S. Liu, and Z. M. Sheng, Phys. Plasmas **22**, 052119 (2015).

[15] H. Y. Zhou, C. Z. Xiao, D. B. Zou, X. Z. Li, Y. Yin, F. Q. Shao, and H. B. Zhuo, Phys. Plasmas **25**, 062703 (2018).

[16] M. N. Rosenbluth, Phys. Rev. Lett. **29**, 565 (1972).

[17] P. N. Guzdar, C. S. Liu, and R. H. Lehmberg, Phys. Fluids B **3**, 2882 (1991).

[18] H. A. Rose, Phys. Plasmas **2**, 2216 (1995).

[19] S. P. Obenschain, C. J. Pawley, A. N. Mostovych, J. A. Stamper, J. H. Gardner, A. J. Schmitt, and S. E. Bodner, Phys. Rev. Lett. **62**, 768 (1989).

[20] T. A. Peyser, C. K. Manka, S. P. Obenschain, and K. J. Kearney, Phys. Fluids B **3**, 1479 (1991).

[21] A. Simon, R. W. Short, E. A. Williams, and T. Dewandre, Phys. Fluids **26**, 3107 (1983).

[22] J. F. Drake, P. K. Kaw, Y. C. Lee, G. Schmidt, C. S. Liu, and M. N. Rosenbluth, Phys. Fluids **17**, 778 (1974).

[23] C. S. Liu, M. N. Rosenbluth, and R. B. White, Phys. Fluids **17**, 1211 (1974).

[24] B. B. Afeyan and E. A. Williams, Phys. Fluids **28**, 3397 (1985).

[25] J. F. Myatt, R. K. Follett, J. G. Shaw, D. H. Edgell, D. H. Froula, I. V. Igumenshchev, and V. N. Goncharov, Phys. Plasmas **24**, 056308 (2017).

[26] R. K. Follett, J. F. Myatt, J. G. Shaw, D. T. Michel, A. A. Solodov, D. H. Edgell, B. Yaakobi, and D. H. Froula, Phys. Plasmas **24**, 102134 (2017).

[27] J. W. Bates, J. F. Myatt, J. G. Shaw, R. K. Follett, J. L. Weaver, R. H. Lehmberg, and S. P. Obenschain, Phys. Rev. E **97**, 061202 (2018).

[28] J. P. Palastro, J. G. Shaw, R. K. Follett, A. Colatis, D. Turnbull, A. V. Maximov, V. N. Goncharov, and D. H. Froula, Phys. Plasmas **25**, 123104 (2018).

[29] R. K. Follett, J. G. Shaw, J. F. Myatt, J. P. Palastro, R. W. Short, and D. H. Froula, Phys. Rev. Lett. **120**, 135005 (2018).

[30] J. W. Goodman, *Statistical Optics* (John Wiley & Sons, Hoboken, NJ, 2015).

[31] T. R. Boehly, R. S. Craxton, T. H. Hinterman, J. H. Kelly, T. J. Kessler, S. A. Kumpan, S. A. Letzring, R. L. McCrory, S. F. B. Morse, W. Seka, S. Skupsky, J. M. Soures, and C. P. Verdon, Rev. Sci. Instrum. **66**, 508 (1995).

[32] D. J. Strozzi, E. A. Williams, A. B. Langdon, and A. Bers, Phys. Plasmas **14**, 013104 (2007).

[33] K. S. Yee, IEEE Trans. Antennas Propagat. **Ap14**, 302 (1966).

[34] P. Colella and P. R. Woodward, J. Comput. Phys. **54**, 174 (1984).